

The impact of baryonic physics on the subhalo mass function and implications for gravitational lensing

Giulia Despali^{1*}, Simona Vegetti¹

¹ *Max Planck Institute for Astrophysics, Karl-Schwarzschild-Strasse 1, 85740 Garching, Germany*

ABSTRACT

We investigate the impact of baryonic physics on the subhalo population by analyzing the results of two recent hydrodynamical simulations (EAGLE and Illustris), which have very similar configuration, but a different model of baryonic physics. We concentrate on haloes with a mass between $10^{12.5}$ and $10^{14} M_{\odot} h^{-1}$ and redshift between 0.2 and 0.5, comparing with observational results and subhalo detections in early-type galaxy lenses. We compare the number and the spatial distribution of subhaloes in the fully hydro runs and in their dark matter only counterparts, focusing on the differences between the two simulations. We find that the presence of baryons reduces the number of subhaloes, especially at the low mass end ($\leq 10^{10} M_{\odot} h^{-1}$), by different amounts depending on the model. The variations in the subhalo mass function are strongly dependent on those in the halo mass function, which is shifted by the effect of stellar and AGN feedback: a lower number of low mass haloes available for accretion in the first place; then additional differences can be attributed to the action of baryonic physics inside the halo. Finally, we search for analogues of the observed lenses (SLACS) in the simulations, doing a selection in velocity dispersion and dynamical properties. We use the selected galaxies to quantify detection expectations based on the subhalo populations in the different simulations, calculating the detection probability and the predicted values for the dark matter fraction in subhaloes f_{DM} and the slope of the mass function α .

Key words: galaxies: halos - cosmology: theory - dark matter - methods: numerical

1 INTRODUCTION

Numerical simulations of galaxy formation are now able to produce realistic galaxy populations, that reproduce observed relations quite well (Vogelsberger et al. 2014; Schaye et al. 2015). Simulations are fundamental to understand the physical properties that shape galaxies and their evolution; while the cold-dark-matter-only simulations and the treatment of the dark matter component, in general, is well established, there is still not a general consensus on how to implement baryonic physics and differences on this side can lead to quite different predictions. Moreover, non standard description of the dark matter component, such as warm dark matter (WDM) models, may also have an important impact (Lovell et al. 2012, 2014; Li et al. 2016).

In this work we analyse the main runs of the EAGLE (Schaye et al. 2015) and Illustris (Vogelsberger et al. 2014) projects, to investigate the effects of different baryonic models on the substructure population. Strong gravitational

lensing allows us to detect directly the presence of substructures either via their effect of the relative flux of multiply imaged quasars (Dalal & Kochanek 2002; Nierenberg et al. 2014) or via their effect on the surface brightness of Einstein rings and lensed arcs (Vegetti & Koopmans 2009; Vegetti et al. 2010, 2012, 2014; Hezaveh et al. 2016). Numerical simulations can then be used to make predictions for the interpretation of observational results, and possibly rule out dark matter and galaxy formation models.

Previous studies concerning subhaloes concentrate mainly on cold dark matter-only simulations, whose results are nowadays well established. Moreover, studies investigating in detail subhaloes and their evolution/distribution in different environments and dark matter/hydrodynamical models usually concentrate on Milky Way haloes, aiming to address the well known “missing satellites” and “too big to fail” problems. The aim of this work is to investigate the effect of baryonic physics on the subhalo population in a wider range of masses and how much subhaloes are affected by the difference in the baryonic physics; we concentrate on

* E-mail: gdespali@gmail.com

haloes between $10^{12.5}$ and $10^{14} M_{\odot} h^{-1}$, which correspond to the halo mass of massive elliptical galaxies (ETGs).

The paper is structured as follows: we describe the simulations and our selection in Section 2. First, we analyse and model the subhalo mass function in the different simulations, concentrating on the difference in the number of subhaloes between the dark matter only and the full hydro runs (Section 3, 4). We proceed by comparing the predictions from simulation with the observational results and what are the probabilities of detecting a substructure given the predictions from different kind of simulations: in Section 5 we select analogues of observed systems and in Section 6 we compare the detection probability inferred from simulations with a real detection in an observational sample (SLACS lenses). Finally, we point out the differences in the baryonic compositions of haloes and subhaloes between the EAGLE and the Illustris simulations in Section 7, that may lead to a different galaxy selection.

2 SIMULATIONS

We choose to analyse the main runs of the EAGLE and Illustris simulations for many reasons. The simulations have comparable box sizes, resolution and starting redshifts; moreover a dark-matter-only counterpart, created with the same initial conditions, exists in both cases and thus constitute an ideal sample for comparison. The main papers from the Illustris (Vogelsberger et al. 2014) and EAGLE (Schaye et al. 2015) collaborations illustrate in detail the differences between the models of baryonic physics, in addition to the differences in the codes - AREPO (Springel 2010) and a modified version of GADGET3 (?), respectively - used to run the simulations. It has been shown that, when looking at the properties of structure in detail, small but significant differences may arise, caused by the simulation code (Heitmann et al. 2008) or even by the halo (Knebe et al. 2011, 2013) and subhalo finders (Onions et al. 2012). These variations become particularly important when we focus on individual structures or small-scale detail. Similar versions of SUBFIND (Springel et al. 2001b) have been used in both simulations to identify structures, eliminating part of these potential differences. Nevertheless, since the baryonic component is treated differently in the two codes, we still expect some effect of the (sub)halo identification (Onions et al. 2012). We make use of the existing SUBFIND catalogues of the two simulations and we concentrate in the mass bin of massive elliptical galaxies (ETGs). In particular, SUBFIND identifies subhaloes as small overdensity peaks within the main halo, which makes it a good candidate for a comparison with lensing.

Due to the resolution limits, the smallest subhaloes have a mass $\simeq 10^8 M_{\odot} h^{-1}$ (with at least 10 particles). We include these subhaloes for statistical purposes, but we caution that reliable measurements require a minimum of 100 particles per subhalo. The regions where particle numbers drop below 100 particles will be marked by a gray region when necessary. Given the good agreement between the two dark-matter-only runs, in this work we show results from the EAGLE dark matter only run (hereafter DMO) for our plots. We use different halo mass definitions throughout this work: (i) we chose M_{200c} is defined as the mass of a sphere centered

on the halo center and enclosing 200 times the critical density ρ_c ($2.77 \times 10^{11} M_{\odot} h^{-1} \text{Mpc}^{-3}$) and we chose it as the main halo mass definition - thus we will refer to this where no other definition is specified ; (ii) M_{fof} is the mass of the group in the halo catalogue identified by the FOF algorithm, which has no pre-defined shape and is usually larger than M_{200c} : this method uses a linking length (conventionally set to $b = 0.2$) to establish which particles belong to the halo; (iii) M_{vir} is defined as M_{200c} , but using the virial overdensity, calculated from the spherical collapse model (Bryan & Norman 1998).

2.1 EAGLE

In this work we analysed the main run of the EAGLE project, created as part of a Virgo Consortium project called the Evolution and Assembly of Galaxies and their Environment (Schaye et al. 2015; Crain et al. 2015; McAlpine et al. 2016) using a modified version of GADGET-3. (Springel et al. 2008). The EAGLE project consists of simulations of Λ CDM cosmological volumes with sufficient size and resolution to model the formation and evolution of galaxies of a wide range of masses, and also include a counterpart set of dark matter only simulations of these volumes. The galaxy formation simulations include the correct proportion of baryons and model gas hydrodynamics and radiative cooling and state-of-the-art subgrid models are used to follow star formation and feedback processes from both stars and AGN. The parameters of the subgrid model have been tuned to match some observational results, as the $z \simeq 0$ galaxy stellar mass function and the observed relation between stellar and black hole mass (Schaye et al. 2015). The main run and its dark matter only counterpart follow 1504^3 dark matter and (in the first case) 1504^3 gas particles in a box size of 100 Mpc, from redshift $z = 127$ to the present time. The cosmological parameters were set to the best fit values provided by the Planck collaboration Planck Collaboration et al. (2014) and are: $\Omega_m = 0.307$, $\Omega_{\Lambda} = 0.693$, $\Omega_b = 0.04825$, $h = 0.677$ and $\sigma_8 = 0.8288$. With this model, the dark matter particle mass is $1.15 \times 10^7 M_{\odot}$ in the dark matter-only run and $9.70 \times 10^6 M_{\odot}$ in the full one, while the initial gas particle mass $1.81 \times 10^6 M_{\odot}$.

The galaxy formation model employs only one type of stellar feedback, which captures the collective effects of processes such as stellar winds, radiation pressure on dust grains, and supernovae and also only one type of AGN feedback (as opposed to e.g. both a “radio” and “quasar” mode). Thus, as detailed below, it differs from the feedback implementation in the Illustris.

2.2 Illustris

The Illustris Project is a series of hydrodynamical simulations of a $(106.5 \text{Mpc})^3$ cosmological volume that follow the evolution of dark matter, cosmic gas, stars, and super massive black holes from a starting redshift of $z = 127$ to the present time. In this work, we used the main run Illustris-1 (and the dark matter only run Illustris-1-Dark), which has a box size of 106.5 Mpc and follows 1820^3 dark matter particles and 1820^3 (initial) gas cells. The simulations were run using the recent moving-mesh AREPO code (Springel 2010). The adopted cosmological model has $\Omega_m = 0.2726$,

$\Omega_{\Lambda} = 0.7274$, $\Omega_b = 0.0456$, $h = 0.704$ and $\sigma_8 = 0.809$, consistent with the WMAP-9 measurements (Bennett et al. 2013). In this case, the dark matter particle mass is $7.5 \times 10^6 M_{\odot}$ in the dark matter-only run and $6.3 \times 10^6 M_{\odot}$ in the full one, while the initial gas particle mass $1.3 \times 10^6 M_{\odot}$. The galaxy formation model includes gas cooling (primordial and metal line cooling), a sub-resolution ISM model, stochastic star formation, stellar evolution, gas recycling, chemical enrichment, kinetic stellar feedback driven by SNe, procedures for supermassive black hole seeding, super massive black hole accretion and merging, and related AGN feedback (radio-mode, quasar-mode, and radiative) and some free parameters constrained based on the star formation efficiency on smaller scale simulations (Vogelsberger et al. 2014). This implementation leads to a stronger AGN feedback with respect to the one in EAGLE. We made use of the data products and the scripts provided in the Illustris data release (Nelson et al. 2015).

3 THE SUBHALO MASS FUNCTION

The subhalo (and also the halo) mass function has been extensively studied in previous works (Giocoli et al. 2008; Springel 2010), which made use of dark matter only simulations. As it is well established that the presence of baryons modifies the halo structure (Schaller et al. 2015), it will also influence the subhalo population, in terms of their number, spatial and mass distribution. A direct comparison between DMO and hydrodynamical simulation with this purpose is quite new (Zhu et al. 2016; Fiacconi et al. 2016) and it is usually done by means of zoom-in resimulations. This technique allows to reach very high resolutions and thus small subhalo masses, but it is intrinsically limited in the number of parent halo and thus does not give statistical predictions on the subhalo mass function. For this last reason, we choose to use the full EAGLE and Illustris simulation: this limits us in resolutions (with the lowest subhalo mass around $10^8 M_{\odot} h^{-1}$), but guarantees that we are taking into account large scale effect such as the total abundance of haloes.

Generally the action of baryons on the overall DM distribution in haloes and subhaloes is threefold: (i) reionization affects the formation and evolution of low-mass haloes, making them almost completely dark (with no star formation) for $M < 10^9 M_{\odot} h^{-1}$; (ii) the DM concentration in the inner region is increased due to gas cooling and adiabatic contraction, both in the haloes and in the most massive subhaloes which host stars; (iii) stellar and AGN feedback cause differences in halo mass, both at the low and high mass end (Cui et al. 2012; Sawala et al. 2013; Vogelsberger et al. 2014; Velliscig et al. 2014; Schaller et al. 2015; Sawala et al. 2015), generally making haloes “lighter” in the hydro runs and thus shifting the halo mass function; finally, different feedback models may affect how matter is stripped from subhaloes. For example, stronger tidal forces in the hydro runs may remove mass more efficiently from subhaloes during their infall (Zhu et al. 2016).

These processes are usually indicated as the causes of the differences in the subhalo mass function between DMO and hydro simulations, implying that the main halo acts differently on its substructures in the two cases - for example both Zhu et al. (2016) and Fiacconi et al. (2016) find a

lower number of substructures in their hydrodynamical simulations. Using the EAGLE and Illustris runs, we want first of all investigate whether the differences in the subhalo population can be related to those in the halo mass function: a different number of haloes available for accretion at redshift z_j would induce a different subhalo mass function at redshift $z_k < z_j$. Then we will proceed to model the subhalo mass function for the mass range of ETGs.

3.1 Halo vs. subhalo mass function

Figure 1 shows the halo and subhalo mass function for both simulations, at four redshifts between 0 and 1. In the upper panel we plot the halo mass function, using all the haloes in the FOF catalogues and, thus, in this case we choose M_{fof} as halo mass; results from the dark-matter-only and full hydrodynamical run are represented, respectively, with solid and dashed lines. In the small lower panels, we highlight the difference between the two cases: by looking at the fractional difference of halo counts between the hydro and the dark matter only run, we notice some similarities and some differences between the two simulations. First of all, both the Illustris and the EAGLE present the predicted lack of small structures in the hydro run, even if at different level. Moreover, while in the EAGLE case, this lack of structure is maintained at all masses, the fraction oscillates in the Illustris, so that there are more intermediate mass haloes in the hydro run and then again less in the high mass tail. This behaviour can be explained as the combined effect of stellar and AGN feedback: they both are less efficient around $10^{11} M_{\odot} h^{-1}$, leaving this masses unaltered and so increasing their abundance due to the contribution of higher masses that are shifted to these lower values. For the Illustris, this is consistent with what is shown in Vogelsberger et al. (2014): comparing the mass of matched haloes they have shown that the mass are reduced by the stellar feedback for low mass haloes and by AGN feedback for high mass ones. For example, neglecting the AGN feedback can lead to an increase of the halo mass function at the massive end (Cui et al. 2012). In the EAGLE simulation the effect of baryonic physics is similar, even if weaker, and for the most massive even the AGN feedback cannot expel enough baryons to reduce the halo mass, so that the ratio tends to 1 (Schaller et al. 2015). In the mass range between 10^{12} and $10^{14} M_{\odot} h^{-1}$, the ratio is similar for the two simulations, leading to a $\simeq 10\%$ reduction.

The second panel of Figure 1 shows the global subhalo mass function, in the same units of the halo mass function. The color scheme is the same; the dot-dashed black curve in the lower panels show the fraction of the halo mass function at $z = 0.2$ from the previous panel, for a more straightforward comparison. We notice a clear relation between the two mass functions: a consistent part of the difference in the subhalo counts between the hydro and dark-matter-only run, can be attributed to the underlying difference in the halo mass function. Having less small structures that can be accreted by larger haloes at any redshift leads to a different number of subhaloes - also enhanced by the fact that not all the small haloes at $z_i < z$ will be accreted. Nevertheless, the residuals do not correspond exactly, and the additional differences can be attributed to the action of baryonic physics, as cooling, adiabatic contraction and tidal forces inside the halo.

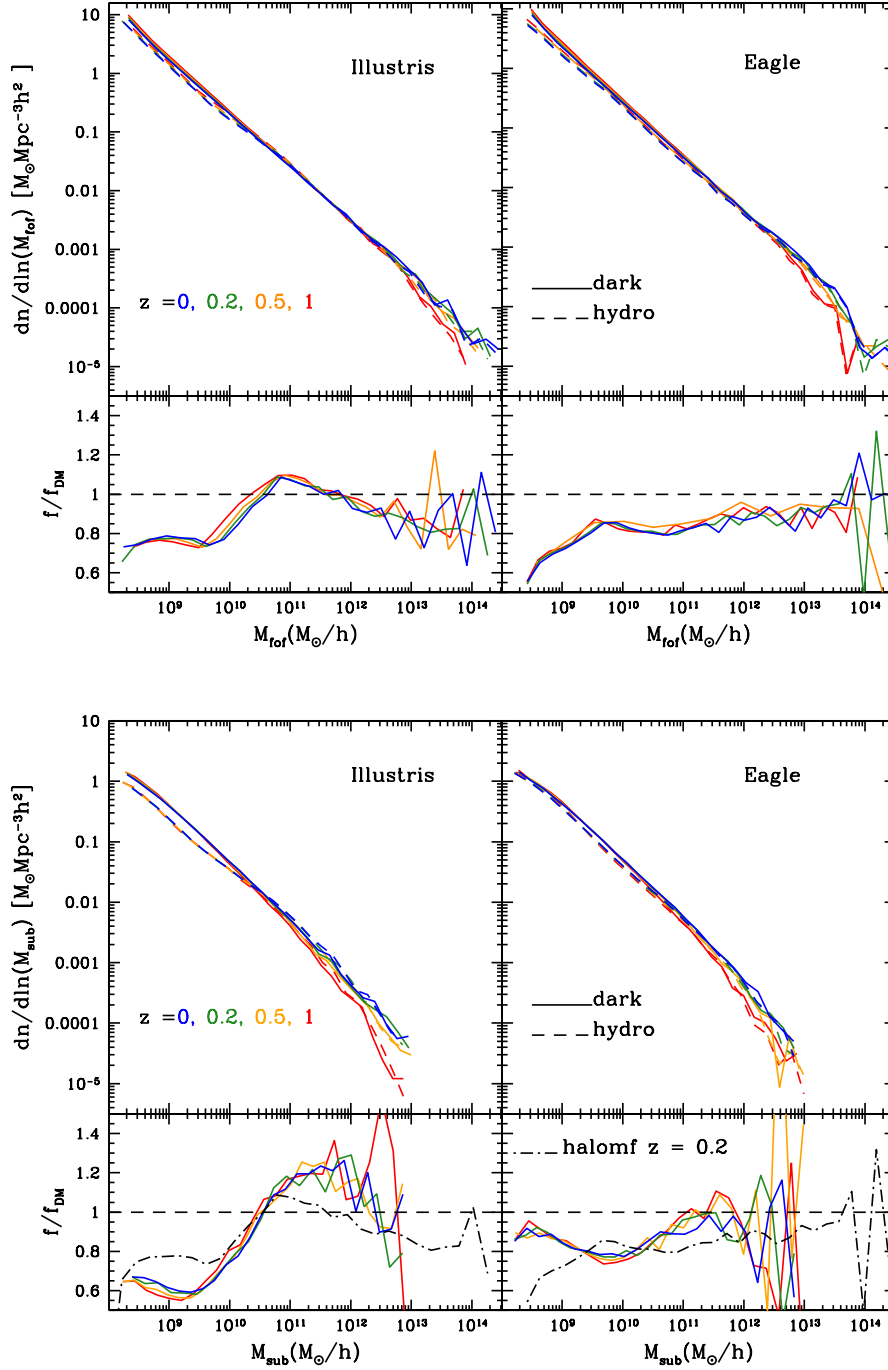


Figure 1. Halo and (global) subhalo mass function in the Illustris and EAGLE simulations - top and bottom panels respectively; the results from the dark matter only and the full hydrodynamical runs are shown respectively by solid and dashed lines and different colors stand for different redshifts ($z=0, 0.2, 0.5, 1$). The lower panel shows the fraction of haloes or subhaloes found in the hydro run, with respect to the dark matter only one. The ratio of the halo mass functions reflect those already found in Vogelsberger et al. (2014) and Schaller et al. (2015).

3.2 Mass bins

We select the dark matter haloes with a mass $M_{200c} = [10^{12}, 10^{14}] M_{\odot} h^{-1}$, consistent with the mass range of massive elliptical galaxies with which we will compare further on in this work. We prefer M_{200c} as the halo mass to the

FOF mass, because it is more easily compared to observational quantities, being associated with a specific radius and shape; thus, we count all the subhaloes within r_{200} and further on we use these definitions, unless specified otherwise. The minimum subhalo mass that we consider is $M \simeq 8.2 \times 10^8 M_{\odot} h^{-1}$, which correspond to $n_{part} \simeq 20 - 30$

Subhalo mass function fit			
sim	α	β	A_M
DMO	-0.9	274	7.4×10^{-4}
EAGLE	-0.85	290	2.1×10^{-4}
Illustris	-0.76	120	2.1×10^{-5}

Table 1. Best fit parameters of the subhalo mass function fit from Equation 1.

depending on the run. Previous work showed that the subhalo identification may not be reliable with less than 100 particles (Onions et al. 2012), which would correspond to $M > 10^9 M_\odot h^{-1}$. Here, we keep the small subhaloes, but we remind that the results for this mass bin must be interpreted with caution.

Figure 2 shows the subhalo mass function in three bins in halo mass, for the two simulations and both the dark-matter-only and hydro run. In the upper panel, we fit our measurements with the model from Giocoli et al. (2010a):

$$\frac{1}{M} \frac{dn(z)}{d \ln m} = (1+z)^{1/2} A_M m^\alpha \exp \left[-\beta \left(\frac{m}{M} \right)^3 \right]. \quad (1)$$

We fit for the parameters (α, β, A_M) , being respectively the slope, the exponential cut-off and the normalization of the curve. For the dark-matter only case we recover the standard value of $\alpha = -0.9$; since the values in Giocoli et al. (2010a) are for virial haloes, the other parameters of our best-fit differs. The best fit parameters are listed in Table 1. Note that the fitting functions are only shifted vertically by the redshift dependence, and thus the residuals between them shifts horizontally in the residual panels, fitting the points well within the errorbars.

The ratio of subhalo counts between the two runs is shown in the lower panels. Different colors stands for different redshifts and the solid black line shows the ratio between the fitting functions. To test whether the residuals depend on the halo mass definition, we re-calculated them also for the whole FOF halo. They are shown by dot-dashed black line in the lower panels (only at redshift $z = 0.2$ to avoid overcrowding), which nicely traces the points calculated with M_{200} . This shows that the lack of small subhaloes in the simulations does not depend only on the distance from the centre, supporting the point that the variation in the halo mass function may dominate over a faster disruption rate inside the halo.

Looking at the errorbars we notice that the difference in fractions between the two simulations is significant only at the low mass end where the number of objects is high enough and therefore the errorbars are smaller. We will explore the low mass end of the subhalo mass function with higher resolution simulations in a follow-up paper: in order to distinguish between the effect of baryons and those from different models of dark matter (such as warm dark matter) we need a good statistic at $10^6 - 10^7 M_\odot$.

4 SUBHALO COUNTS

In this Section we present and model the distribution of subhaloes as a function of radius, both in terms of their

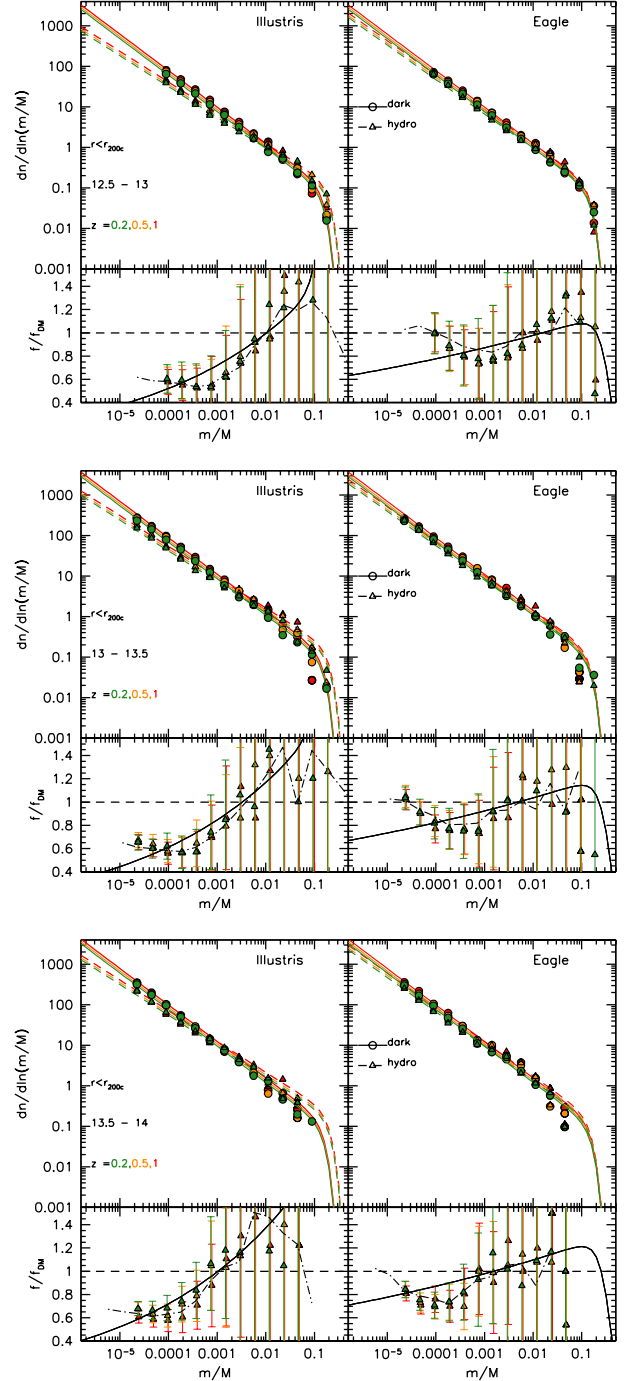


Figure 2. Subhaloes mass function for three bins in halo mass in our sample ($m/M = m(\text{subhalo})/M_{200c}$). The colour scheme is the same of Figure 1. *Main panels:* circles and triangles show our measurements for the dark and hydro simulations, fitted by the curves coming from Equation 1 (again solid and dashed lines). *Inset panels:* fraction of haloes or subhaloes found in the hydro run, with respect to the dark matter only one - with poissonian errors. While the points stand for the fractions calculated from the data, the solid black line shows the ratio between the fitting functions: as they scale only with redshift for a given mass bin, this is the same for all the three considered redshifts. The ratio between measurements taken inside the whole FOF group - instead of r_{200c} - is represented by the dot-dashed black line. The gray region correspond to subhaloes with less than 100 particles.

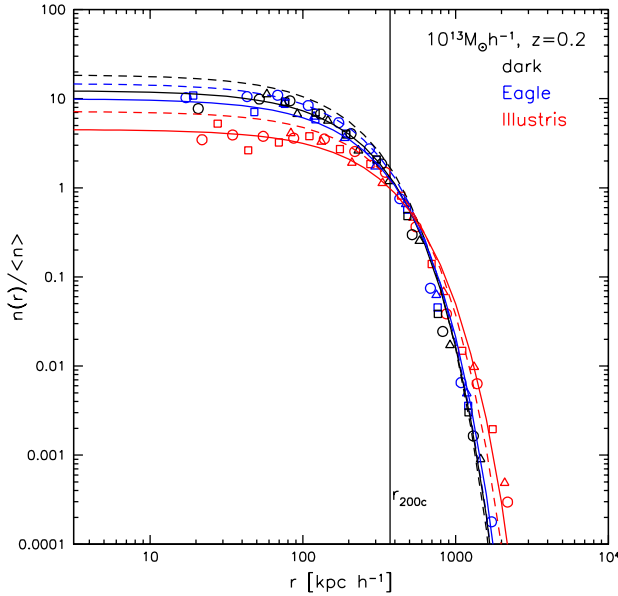


Figure 3. Number of subhaloes as a function of radius. As in (Springel et al. 2008), the radial distribution of subhaloes can be well fitted by an Einasto profile. Different point types indicate three bins of subhalo masses - 10^8 (circles), 10^9 (squares) and $10^{10} M_{\odot} h^{-1}$ (triangles): all these subhaloes lie on the same curve, when the number is normalized by the mean density of subhaloes of that specific mass bin within r_{200c} . Solid lines show the best fit Einasto profile to the $z = 0.2$ points, while the same fit for $z = 0.5$ (for which we do not show the points) are given by the dashed lines. Other mass bins give similar results, and we provide the parameters of the Einasto fits in Table 2.

sim	10^{13}	$10^{13.5}$	10^{14}
$z = 0.2$			
DMO	(1.79 , 309)	(2.12 , 436)	(1.12 , 881)
EAGLE	(1.62 , 330)	(1.92 , 447)	(1.04 , 895)
Illustris	(0.732 , 438)	(1.04 , 488)	(1.11 , 760)
$z = 0.5$			
DMO	(2.74 , 291)	(3.23 , 388)	(1.17 , 381)
EAGLE	(2.4 , 306)	(4.38 , 360)	(1.61 , 514)
Illustris	(0.732 , 438)	(2.02 , 733)	(2.02 , 677)

Table 2. Best fit parameters of the Einasto fit to the number of subhaloes as a function of radius. For each redshift-mass-simulation combination, we give the values of (ρ_s, r_s) of the fit; we find that in all cases $\alpha = 1.1$ works well. Some of the fitting functions are shown in Figure 3, together with the points.

three dimensional number density and in projection. As we adopted M_{200c} as halo mass, we use r_{200c} accordingly.

It has been shown in previous work (Springel et al. 2008) that the number of subhaloes as a function of radius can be fit with an Einasto profile:

$$\rho(r) = \rho_s \exp \left\{ -\frac{2}{\alpha} \left[\left(\frac{r}{r_s} \right)^{\alpha} - 1 \right] \right\} \quad (2)$$

In Figure 3 we show the radial distribution of subhaloes:

all the subhaloes lie on the same curve, when the number is normalized by the mean density of subhaloes of that specific mass bin within r_{200c} . Solid lines show the best fit Einasto profile to the $z = 0.2$ points, while the same fit for $z = 0.5$ (for which we do not show the points) are given by the dashed lines. In all cases, we find that our points are well fitted by an Einasto profiles with $\alpha = 1.1$, while the values of normalization ρ_s and scale radius r_s vary with mass and redshift. In Table 2 we provide the best-fit values for each combination of redshift, mass bin and simulation. At fixed redshift, increasing the mass corresponds to a horizontal shift in the profiles (i.e. an increased number of subhaloes at larger distances); on the contrary, at fixed mass, increasing z leads to an increase in the normalization (i.e. an overall increased number of subhaloes). We also note that for high masses, the three profiles have more similar shapes, indicating that the effect of baryons is less important in this mass range.

Figure 4 shows the subhalo counts as a function of distance from the centre in three and two dimensions, for haloes of mass $M_{200c} \simeq 10^{13} M_{\odot} h^{-1}$ at redshift 0.2 and 0.5. We compare the dark matter only results, the EAGLE (blue open triangles) and the Illustris (red open squares) hydrodynamical simulations. The left panels show the three dimensional subhalo counts within r_{200c} , expressed as number of subhaloes per $(kpc/h)^{-3}$. The general trend is very similar for all the simulations, but we note again a different effect of the two models of baryonic physics: in the Illustris simulation, the lack of subhaloes is again more evident than in EAGLE, reflecting what could be inferred from the subhalo mass functions. In projection (right panel), the distribution flattens and maintains the same ordering, similarly to what found in Xu et al. (2015) - this time we plot only the subhalo counts within $0.3 \times r_{200}$, because only the central parts of the halo are relevant for lensing; counts are expressed both in units of $(kpc/h)^{-2}$ and $arcsec^{-2}$. Projecting all the substructures inside the FOF group gives a slightly different results in the higher subhalo mass bin; this is explained by the fact that bigger subhaloes are found in the outer region of haloes and the FOF group is more extended than r_{200c} . On the contrary, the average number is not significantly different for small subhaloes.

5 A COMPARISON WITH OBSERVED LENSES

5.1 The SLACS survey

The Sloan Lens ACS (SLACS) Survey is an efficient Hubble Space Telescope (HST) Snapshot imaging survey for new galaxy-scale strong gravitational lenses (Bolton et al. 2006). The SLACS survey is optimized to detect bright early-type lens galaxies with faint lensed sources in order to increase the sample of known gravitational lenses suitable for detailed lensing, photometric, and dynamical modeling. SLACS has identified nearly 100 lenses and lens candidates, which have a stellar mass ranging from $10^{10.5}$ to $10^{11.8} M_{\odot}$ (Auger et al. 2009) and estimated total masses of the order of $10^{13} M_{\odot}$ (Auger et al. 2010a), at redshift $z \simeq 0.2$ - spanning approximately $0.06 \leq z_{lens} \leq 0.5$ for the lenses and $0.2 \leq z_{lens} \leq 1.3$ for the source. They can be considered

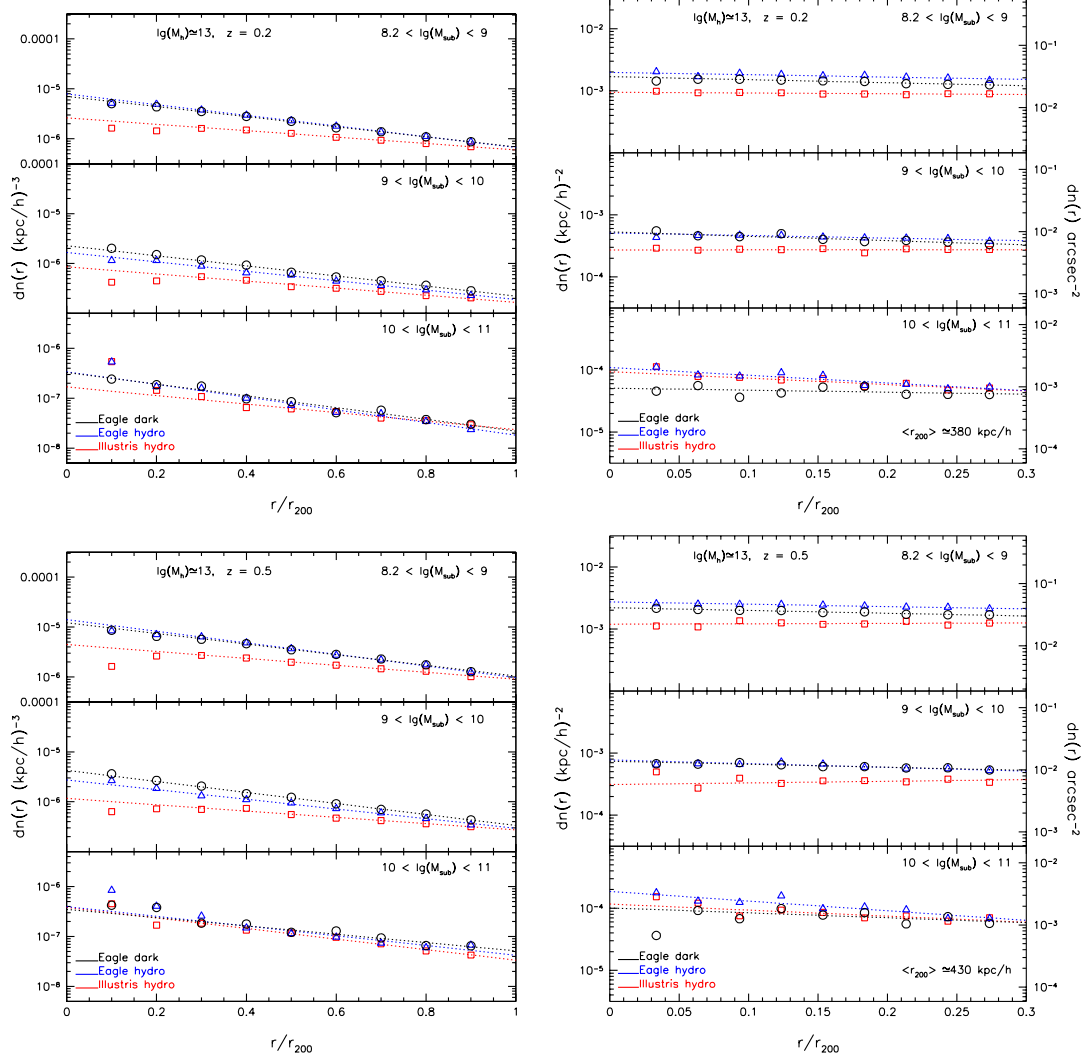


Figure 4. Subhalo counts at redshift $z = 0.2, 0.5$. (*Left*) 3D number of subhaloes, in units of physical $(kpc/h)^3$. (*Right*) projected number of subhaloes, in units of physical $(kpc/h)^2$ or $arcsec^2$. In all the panels, we divide the subhaloes in three mass bins, to show how the abundance scales of approximately one order of magnitudes for each decade in mass. Results for the DMO, EAGLE and Illustris hydro runs are represented respectively by black circles, blue triangles and red squares; the dotted lines are linear best fit relations to the points.

representative of the population of massive elliptical galaxies with stellar masses $M_* \geq 10^{11} M_\odot$ (Auger et al. 2009).

In this paper, we make use of the results from Auger et al. (2009, 2010a,b), in order to select SLACS-like candidates in the EAGLE and Illustris hydro simulations.

5.2 Considerations on the IMF

Even though it could seem more straightforward, selecting the simulated galaxies in terms of the total value of stellar mass may present some problems concerning the chosen IMF: the SLACS total stellar masses have been calculated by Auger et al. (2009), using both the Chabrier and the Salpeter IMF and the latter has been shown to be the preferred model; Auger et al. (2010a) also ruled out a Chabrier mass function when calculating the total halo mass. On the other hand, both the EAGLE and Illustris simulations have been run with a Chabrier IMF and rescaling the mass with

the usual relation $M_{Sa} = M_{Ch}/0.55$ would not yield to a meaningful comparison: changing the IMF in the simulation code would require modification in the baryon and subgrid models, leading to more complicated differences than a simple rescaling. For this reason, following Xu (2016), we avoid a selection in total stellar mass and prefer to use dynamical measurements and velocity dispersion; we will then go back to stellar masses to show the range of objects that we select in this way. This presents another advantage: as can be seen in Figure 6, the stellar mass of the central galaxy is on average different in the two simulations for a halo of a given total mass and so using it as a main selection criterion could enhance the difference in total mass between the two samples.

5.3 Selection of SLACS analogues

In order to select analogues of the SLACS lenses from the considered simulations, we started by excluding all haloes which are clearly unrelaxed: we excluded those for which the distance between the halo centre of mass and the position of the minimum of potential is more than 5% of the radius, as they may be composed by multiple components and are not suitable for our selection (Neto et al. 2007; Ludlow et al. 2012).

We then apply a dynamical selection, identifying the galaxies that are most probably ellipticals, or at least bulge dominated. This kind of information comes from dynamical measures already present in the EAGLE and Illustris catalogues, which allow to distinguish the disk and bulge components and give very similar informations and results. For the EAGLE run we use the amount of stellar mass within 20 kpc that rotates in the opposite sense to the rest of the galaxy: this component should be approximately one half of the bulge mass, since the disc will rotate entirely in the same sense as the galaxy as a whole; thus subtracting it the total mass within 20 kpc, we can get the disk mass. We discarded the objects for which the disk fraction exceeds 50%. For the Illustris run, the dynamical selection is based on the specific angular momentum (Teklu et al. 2015; Snyder et al. 2015) through the parameter $\epsilon = J_z/J(E)$, where J_z is the specific angular momentum and $J(E)$ is the maximum angular momentum of the stellar particles at positions between 50 before and 50 after the particle in question in a list where the stellar particles are sorted by their binding energy. This quantity has been calculated for each stellar particle and we know:

- the fraction of stars with $\epsilon > 0.7$, which is a common definition of the disk stars - those with significant (positive) rotational support
- the fraction of stars with $\epsilon < 0$, multiplied by two, which in turn commonly defines the bulge.

Following Teklu et al. (2015), the galaxy is disk dominated if the first quantity is greater than 0.4 and bulge dominated if the second one is larger than 0.6. Our selection combine these two criteria, with the second one being much more restrictive than the first. Despite the fact that the quantities calculated for the two simulations are different, the resulting selection is similar: both criteria allow us to estimate the mass of the disk/bulge of the galaxy and with these informations ruling out systems which clearly possess a disk works well.

Among the galaxies identified by the dynamical selection, we then choose galaxies that have a velocity dispersion similar to that of the SLACS lenses (160-400 km/s). This is calculated within half of the effective radius r_e , which traces half of the light. For the simulated galaxies, we calculated a projected half mass radius, using the central galaxies corresponding to our selected haloes, averaging over the three projections along the axes. This quantity should be a good counterpart of the effective radius and we use it also to recalculate the velocity dispersion.

Figure 5 illustrates the result of our selection for SLACS in the $r_e - M_*$ space, showing all the galaxies (selected only in halo mass $M_{200c} = 10^{12} - 10^{14} M_\odot h^{-2}$ and relaxation) in the upper panel and the selected analogues in the bottom

one. The SLACS lenses are represented by the black circles (open for Chabrier IMF and filled for Salpeter), while the simulated galaxies in red (open squares) and blue (open triangles), for the Illustris and EAGLE simulations respectively. These come from three snapshots of the simulations - the closest to the z range of the SLACS and the closest to each other. As has been found in Auger et al. (2010b), the SLACS lenses are well fit by a linear relation in the $M_* - r_e$ space, represented by the dashed and solid black line for the two IMF. The bottom panel of Figure 5 then show the selected sample, using dynamical properties and velocity dispersion, proving that we are able to choose in simulations objects very similar to the SLACS lenses. The main restrictions are given by the dynamical criteria: this reinforces the statement that SLACS are representative of the whole ETGs population at these redshifts.

5.4 Properties of the selected sample

We investigate other similarities of the observed galaxies with the sample from simulations. Auger et al. (2010a) provide a relation to estimate the virial mass, based on a model that relates the virial and stellar masses (Moster et al. 2010), for various combinations of IMF (Chabrier, Salpeter and a Free model) and halo profile (NFW and two profiles from Blumenthal et al. (1986) and Gnedin et al. (2004) that take into account cooling and adiabatic contraction which give very similar results). This models defines virial mass as the mass enclosing the virial overdensity, as calculated from the spherical collapse model (Bryan & Norman 1998). It is defined in the same way as in simulations; we use the virial mass for the SLACS lenses calculated for Salpeter IMF and profile from Gnedin et al. (2004). In Figure 7 we show the stellar and virial mass distributions of SLACS and of the selected sample of galaxies, finding a good agreement. Here we note that the virial mass of the two simulations peak at slightly different values, while stellar masses show a better agreement, bringing us back to the fact that Illustris has a higher stellar mass at fixed halo mass (Figure 6). Nevertheless, it is possible to identify a good sample of analogues in both cases. In the bottom panel, we show the agreement between the data and the sample selected from simulations for what regards magnitudes, finding a good agreement. As discussed in Xu (2016), who selected lens analogues in a similar way in the Illustris simulation, simulated early type galaxies selected through velocity dispersion lie well on the fundamental plane.

6 COMPARISON WITH A REAL DETECTION

In this section we will quantify the probability of detecting substructures in SLACS-like lenses. Among the whole SLACS sample, 11 objects have been selected on a signal to noise basis and have been modelled searching for the presence of substructures (Vegetti et al. 2014). In this sample, only one lens has shown evidence of one substructure (Vegetti et al. 2010), while in the other cases non-detections can still be used as important informations. Our aim is to compare this rate of detections with a prediction from simulations. We will then calculate the fraction of dark matter in

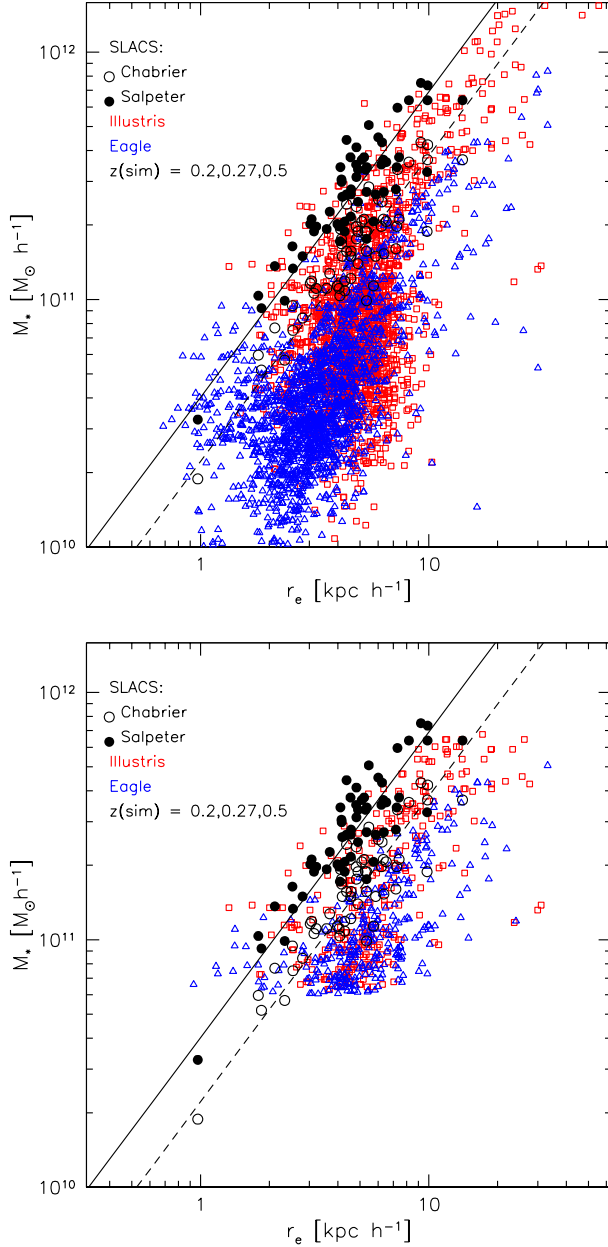


Figure 5. *Top:* Total stellar mass vs. effective radius, for the SLACS lenses (black filled circles for Salpeter IMF and open circles of Chabrier IMF) and the galaxies in the EAGLE (blue open triangles) and Illustris (red open squares) simulations. The black solid (dashed) line shows the best fit to the SLACS data (Auger et al. 2010b) for the Salpeter (Chabrier) IMF. Here we show all the galaxies that lie in the $M_{200c} = 10^{12} - 10^{14} M_{\odot} h^{-1}$ mass bin. *Bottom:* same for the galaxies selected through dynamical properties and velocity dispersion ($\sigma_v = 160 - 400 \text{ km/s}$).

subhaloes f_{DM} from a sample of 11 lenses and compare it with that inferred from observations.

6.1 Detection probability

In order to determine the probability of one detection in a sample of 11 lenses, we extract 11 random haloes from our selections and project their substructures on the image of

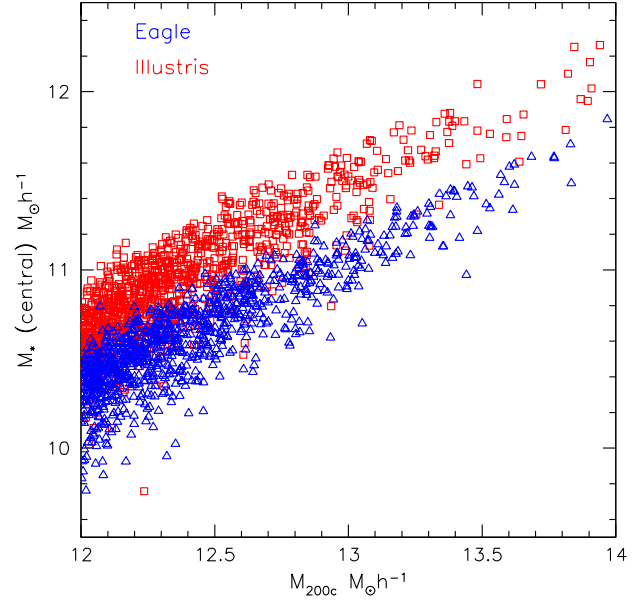


Figure 6. Stellar mass of the central galaxy vs. the total mass of the halo.

each lens. We repeat the procedure 600 times for each case (pure dark matter, EAGLE or Illustris hydro), to ensure a good statistic. We find that a substructure - with any mass larger than $10^9 M_{\odot} h^{-1}$ - is present in the sample of 11 lenses and in the area around the Einstein rings where it could affect the lensing signal in around 41%, 37% and 18% of the cases, respectively for dark-matter only, EAGLE and Illustris. Among these, probabilities are higher for low mass substructures, since - as seen in Figure 4 - the scaling between density and mass is of one order of magnitude for each decade in mass.

As detailed in Vegetti et al. (2014), counting how many substructures lie in the right region is not enough, because the possibility of detecting a substructure is not independent of its location: the effect of the substructure would be more evident for structured sources and in a location where a perturbation of the surface brightness could be stronger. In order to verify how many substructures can actually be detected, we make use of the sensitivity function maps created by Vegetti et al. (2014): these provide the minimum mass that could be detected for each pixel of each of the 11 lenses. After projecting and counting the simulated subhaloes, we associate them with a pixelized grid with the same spacing of the sensitivity function and we compare the mass of the substructure with the sensitivity of the particular pixel it falls in: if the lowest detectable mass in that pixel is lower than the subhalo mass, then we consider it a detection, otherwise it is listed as non-detection. This leaves us with an overall probability of detecting one substructure with mass $M > 10^9 M_{\odot}$ in one lens (and nothing else in the others) 20%, 19% and 10% in the three cases, meaning that nearly 50% of subhaloes are projected onto a pixel that is not sensitive enough to detect them. Figure 8 shows the average number of detected subhaloes with a mass larger than $10^9 M_{\odot} h^{-1}$ per sample of 11 objects, as a function of subhalo mass; probabilities in wider mass bins are summarized

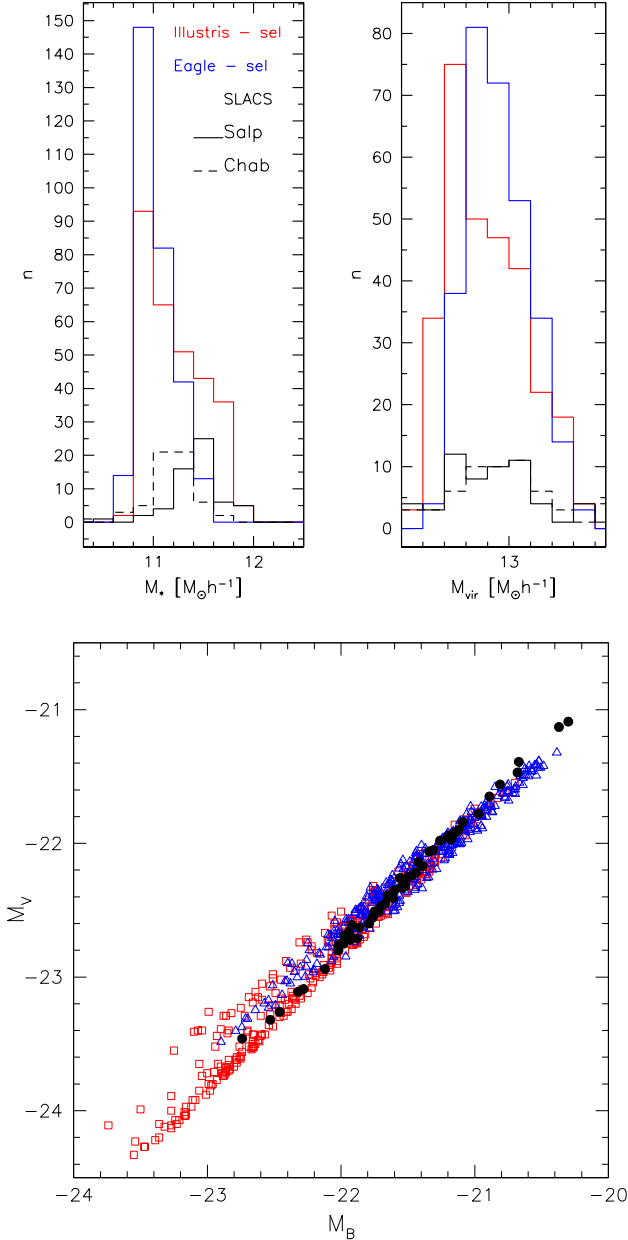


Figure 7. *Top:* distribution of stellar mass and virial mass for the SLACS galaxies and the samples selected in the simulations; here we plot the number of objects found in each case: we have more simulated than observed galaxies, but the ranges of stellar and virial masses recovered by the selection procedure are in good agreement. *Bottom:* relation between B and V magnitudes for the SLACS lenses and the galaxies selected from simulations.

in Table 3. These results are compatible with the projected number counts of Figure 4, which are then further reduced by considering the sensitivity function. We point out that the sensitivity functions have been calculated using a 10σ detection as threshold: using weaker constraints may lead to higher detection probabilities from simulations.

Figure 9 show two examples of substructures projected on the sensitivity function of the lens galaxy SDSSJ0946+1006, where there has been a real detection (Vegetti et al. 2010). In both panels the black point shows

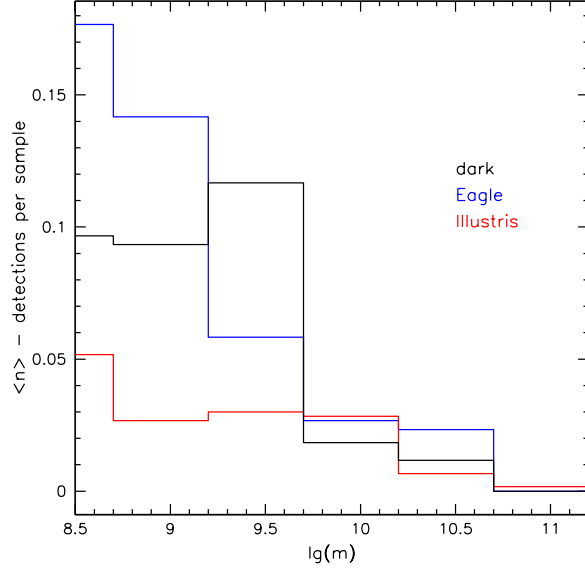


Figure 8. Average number of detected subhaloes per sample of 11 objects, as a function of subhalo mass. The gray region indicates again where subhaloes have less than 100 particles.

percentage of detections using sensitivity functions			
range [$M_\odot h^{-1}$]	DMO	EAGLE	Illustris
$M > 10^9$	20	19	10
$10^9 < M < 10^{10}$	18.5	17	8
$M > 10^{10}$	1.5	2	2

Table 3. Probability of detecting one substructure of a certain mass in a sample of 11 SLACS-like lenses, taking into account the effect of the sensitivity function. Figure 8 shows a more detailed distribution of the percentage of detections. All these values are extracted from 600 random samples from each simulation.

an example of detection: in the left panel the detected mass is $1.6 \times 10^9 M_\odot$ - very similar to the real detection in this region, while in the right panel is $7 \times 10^8 M_\odot$. The white dots show a non-detection and a substructure that does not fall in the right region.

6.2 Estimate of f_{DM}

Apart from projecting the substructures of the analogues on the sensitivity function, we also used our selection to calculate the mass fraction in subhaloes. We calculate the total projected dark matter mass in the area of the sensitivity functions, projecting the dark matter particles. For each of the selected haloes, we considered three independent projections for each of the 11 sensitivity functions. The resulting projected dark matter masses are generally consistent with those calculated for this sample of 11 SLACS lenses and on average of the order of $2.5 \times 10^{10} M_\odot h^{-1}$. We then calculate the expected number of subhaloes $dn/(kpc/h)^2$, as in Figure 4 for subhaloes with masses between 10^8 and $5 \times 10^9 M_\odot h^{-1}$; since this scales approximately of one order of magnitude for each decade in mass, we extrapolate the

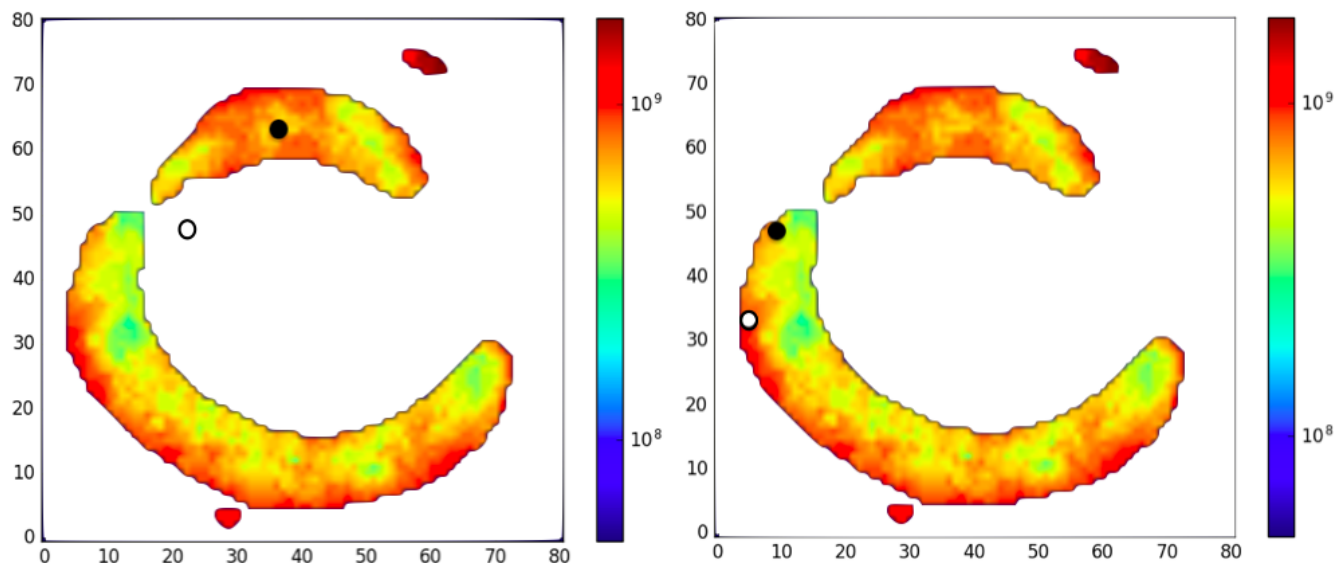


Figure 9. Examples of the projection of subhaloes on the sensitivity function (lens galaxy SDSSJ0946+1006). The color scale indicates the minimum subhalo mass that can be detected in each pixel in the region around the Einstein radius (in M_\odot). In both panels the black point shows an example of detection: in the left panel the detected mass is $1.6 \times 10^9 M_\odot$ - very similar to the real detection in this region, while in the right panel $7 \times 10^8 M_\odot$. The white point in the left panel is a non-detection: the subhalo mass is $2.2 \times 10^8 M_\odot$, thus too low to be detected in that region. Finally, the white point in the right panel shows a case in which the subhalo falls in the central part of the halo but not in the region around the Einstein radius (it had a mass of $9 \times 10^8 M_\odot$).

expected number of lower mass subhaloes between 10^6 and $10^8 M_\odot h^{-1}$ that we do not resolve in the simulations; subhaloes in this mass range are on average completely dark and so we can use their counts to estimate the dark matter fraction in subhaloes. We then used the total projected dark matter mass and the number density of subhaloes in the sensitivity function areas, obtained multiplying the mean value for the total area. The mean densities in substructures in the range $4 \times 10^6 - 4 \times 10^9 M_\odot h^{-1}$ and the resulting mean mass fraction in substructures on the areas of the sensitivity functions are listed in Table 4. For the dark matter only case we are consistent with a value of f_{DM} compatible with Vegetti et al. (2014) - and thus consistent with the predictions from Xu et al. (2015). The mass fraction in substructure in the range $10^6 - 10^9 M_\odot h^{-1}$ is then lower for the simulations with baryons and especially for the Illustris simulation. These values, combined with the best fit slope of the subhalo mass function α can be used to fully constrain the subhalo mass function and can be compared with those inferred from observations. Vegetti et al. (2014) found a mean substructure projected mass fraction of $f_{DM} = 0.0076^{+0.0208}_{-0.0052}$ for a uniform prior on α and $f_{DM} = 0.0064^{+0.0080}_{-0.0042}$ for a gaussian prior with mean 1.9 and standard deviation 0.1. Thus, the values of (f_{DM}, α) from the DMO and from the EAGLE hydro runs are compatible with their findings within the errors, both for the mass fraction f_{DM} and the slope α . The results from the Illustris hydro run instead do not lie within the errors. We compare with this prediction and not with those of Vegetti et al. (2010) and Vegetti et al. (2012), since the first included only one lens and the second takes into account another lens which is not part of the SLACS sample, coming from a sample selected in a different way, with a different redshift and mass.

sim	subhalo mass fraction	
	$\langle \rho_{sub} \rangle [M_\odot h/kpc^2]$	f_{DM}
DMO	5.826×10^6	0.0044 ± 0.0018
EAGLE	3.858×10^6	0.0025 ± 0.0012
Illustris	1.541×10^6	0.0012 ± 0.0004

Table 4. Average projected mass density in subhaloes on the areas of the sensitivity function, for the simulated analogues of SLACS lenses.

7 STRUCTURE OF SUBHALOES

To conclude, we look at the structure of subhaloes and host haloes in the full hydrodynamical runs for the lens analogues. SUBFIND identifies the main “smooth” component of the FOF halo as the first and most massive subhalo, followed in the catalogue by all the smaller structures. In Figure 10 we distinguish the main halo and its subhaloes and study their baryonic content: we plot the average percentage of mass built up by stars and gas, respectively in orange and green. The right panel shows the composition of the central subhalo (i.e. the main halo) for the two simulations, at redshifts 0.2 and 1. The results from the two simulations present significant differences: in the EAGLE run, the main halo contains much more gas than in the Illustris and at the same time less gas is bound to the subhaloes. Moreover, we note again an higher stellar mass in ILLUSTRIS galaxies, as in Figure 6. As shown in Schaye et al. (2015), the star formation is higher in the Illustris simulations for all masses and the feedback model induces a stronger AGN feedback, which expels almost all the gas from the halo with the purpose of quenching star formation - and is one of the known problems of the Illustris recipe. The effect of different feedback

models on the baryon and gas fractions has been studied in Velliscig et al. (2014), who found an important depletion in the presence of an AGN. A selection of the simulated galaxies using observational constraints (as stellar mass, effective radius or magnitude) may thus be affected by the different composition of the central halo, as we will detail in Section 7.

The left panels show the same for the subhaloes, binned by halo mass (different columns) and distance from the centre: the subhaloes which lie in the very centre of the halo - closer than $0.3 \times r_{200}$ - are represented by solid lines, while the others - between $0.3 \times r_{200}$ and r_{200} - by dotted lines. First of all, we find - as in previous works - that the smallest subhaloes ($10^8 - 10^9 M_\odot h^{-1}$) are almost completely dark and do not form stars. Moreover, subhaloes which lie near the centre lost the majority of their gas, so that stars build up to 40 % of the total mass, while more distant satellites show fewer signs of stripping.

Figure 11 and 12 show mean radial density profiles of the central halo and of the subhaloes in corresponding bins. The mean density profile of the central is very similar in the two cases (Figure 11) : stars and gas behave differently, but their contributions sum up to give a comparable total density profile. Subhalo profiles (Figure 12) show clearly the effects of accretion and disruption: in every mass bins, those closer to the centre are less extended. Nevertheless, subhaloes of the same mass preserve a very similar shape towards the centre, despite the different distance from the centre of the main halo. The subhalo density profiles in EAGLE are steeper with respect to the Illustris ones, especially for high-mass subhaloes (in the two right-hand columns of Figure 12), which host more stars and whose profiles can be traced better. This could be attributed to a stronger stellar feedback in the latter one, able to flatten the central part of the profile (Duffy et al. 2010) and which could act also in the high mass subhaloes, or due a stronger tidal disruption. Without resimulating the same structures with the two codes, it is hard to identify the exact mechanism that causes the difference. Nevertheless, pointing out possible systematic differences is important, as subhalo concentration plays a role in the possibility to observe them through gravitational lensing. We plan to analyse subhalo profiles and concentration in detail in a follow-up paper, using ray-tracing to model their influence on the lensing signal.

8 SUMMARY

We have analysed the results of the two most recent simulations (EAGLE and Illustris), aiming to characterize the subhalo population in simulations with different baryonic physics models. We concentrate on haloes mass between $10^{12.5}$ and $10^{14} M_\odot h^{-1}$ and redshift between 0.2 and 0.5, since we want to compare with observations of ETGs at these redshifts. Here we summarise our main results, regarding the modelling of simulations:

- the presence of baryons modifies the abundances and structure of haloes, through processes such as adiabatic contractions, cooling, stellar and AGN feedback. As a consequence, the subhalo population is affected (i) by the different abundance of haloes in the field that can be accreted

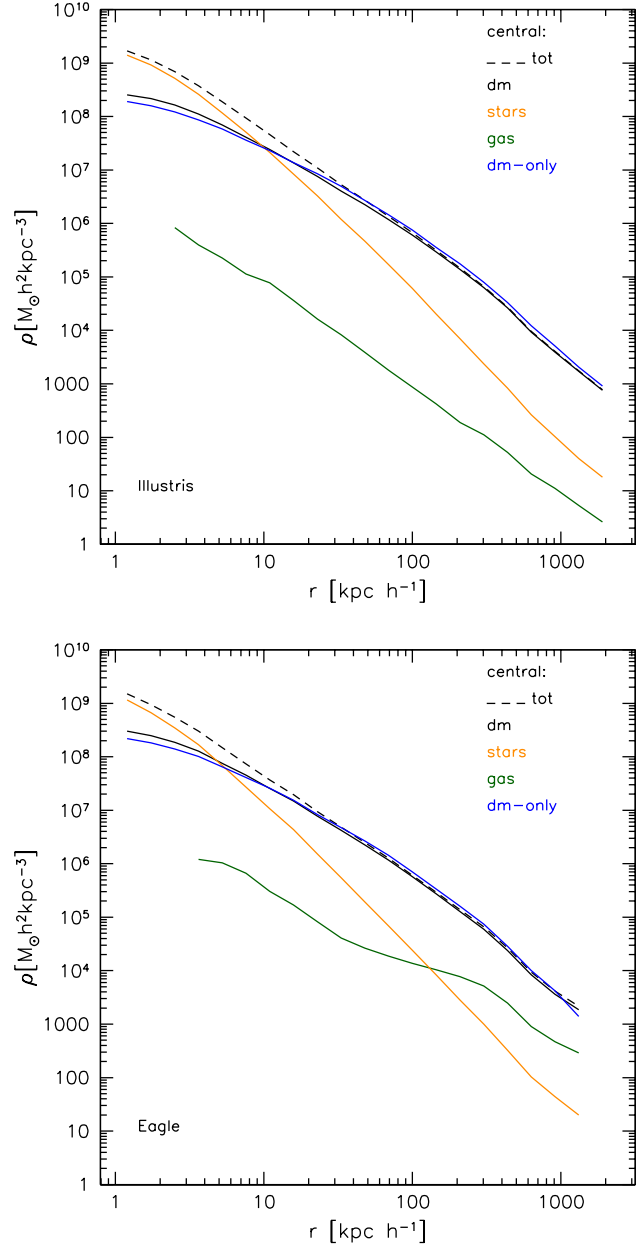


Figure 11. Mean density profile of the central halo (without subhaloes). We chose 10 haloes from each of the two hydro runs: they have $M_{200c} \simeq 10^{13} M_\odot h^{-1}$ and very similar dynamical properties; the central galaxy has been identified as a massive elliptical through a selection process that is described further on in this work (Section 6). We show the profile of each component (dark matter - black, stars - orange, gas - green) and the total density profile in black dashed lines. The blue curve shows the profile of the counterparts of these haloes in the dark matter only run. As from Figure 10 the central halo from EAGLE contains more gas, while the one from Illustris has a bit more stars; nevertheless, the total and the dark matter profiles are very similar.

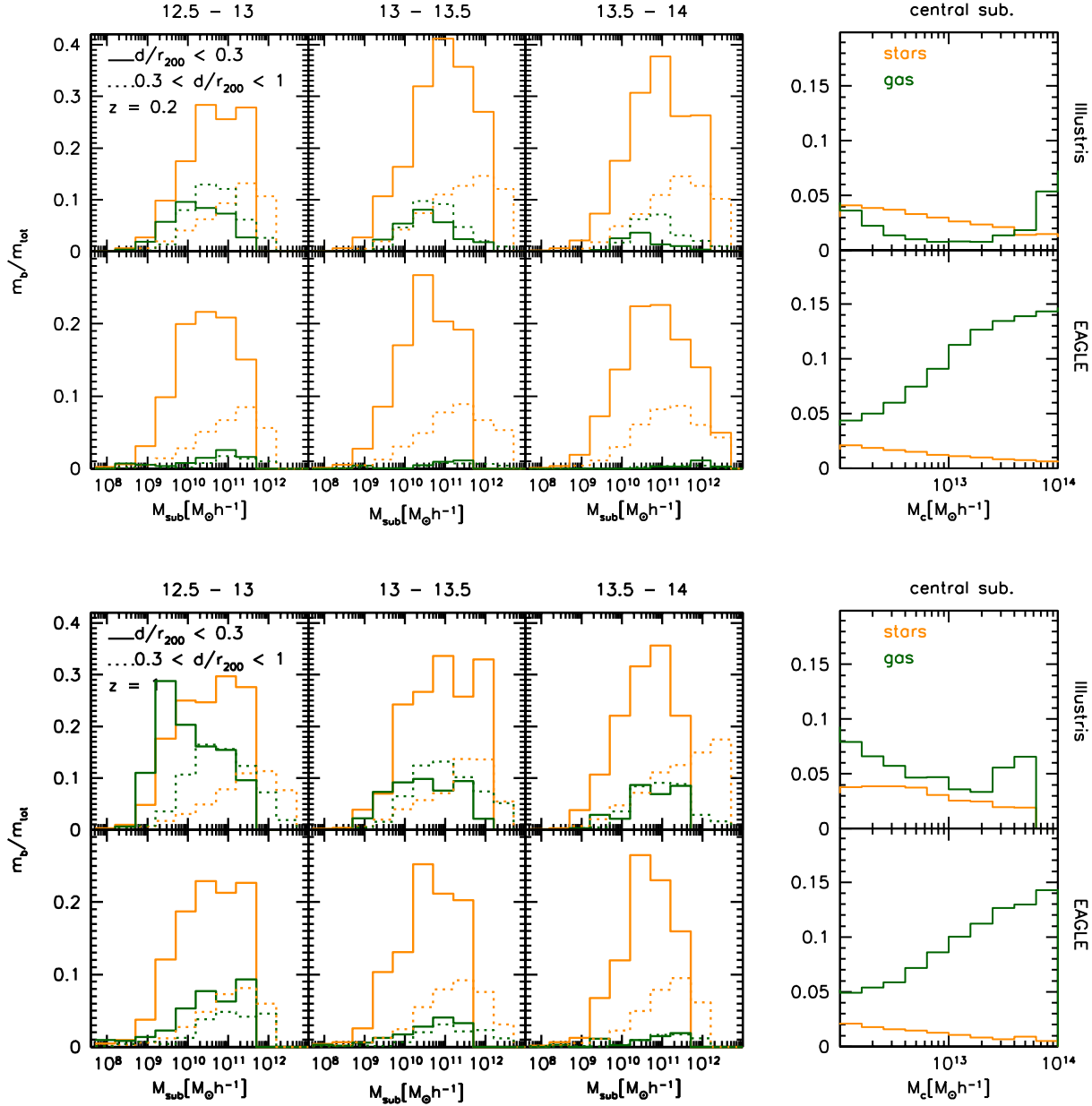


Figure 10. *Left:* subhalo composition. In all panels the orange and green lines show, respectively, the mass fraction in star and gas of the subhaloes. Subhaloes are binned according to the mass of the parent halo; each column shows the results for one of the three bins ($12.5 \leq \lg(M_{200}) \leq 13$, $13 \leq \lg(M_{200}) \leq 13.5$ and $13.5 \leq \lg(M_{200}) \leq 14$). Subhaloes are also divided according to their distance from the centre of the halo: solid lines show those which lie within 30% of the radius r_{200} , while dotted lines those which are found within $0.3r_{200}$ and r_{200} . *Right:* composition of the central halo (first subhalo or smooth component of the halo).

by larger haloes and (ii) by a different dynamic and survival of substructure inside the main halo. Depending on the adopted physical model, the depletion in the low-mass end of the subhalo mass function changes: in the EAGLE hydro run, we find $\simeq 20\%$ fewer subhaloes with a mass between 10^8 and $10^{10} M_\odot$, while for the Illustris simulation this percentage can be as high as 40%. A different effect is present also at higher subhalo masses ($10^{11} - 10^{12} M_\odot$), where Illustris shows an excess of subhaloes in the hydro run, which is not present in EAGLE (Figure 1); this kind of differences need to be investigated more since they may be similar to those

caused by warm dark matter models (Lovell et al. 2014; Li et al. 2016) at the low mass end.

- We model the subhalo mass function for different halo masses, using a relation from Giocoli et al. (2008); for the DMO case, we find a slope $\alpha = -0.9$, consistent with previous studies, while we find shallower slopes for the hydro runs, with $\alpha = -0.85$ for the EAGLE hydro run and $\alpha = -0.76$ for the Illustris one (Figure 2);

- the projected number density of subhaloes is quite flat as a function of radius, as shown already in Xu et al. (2015) for a different mass range; the abundance of subhaloes that

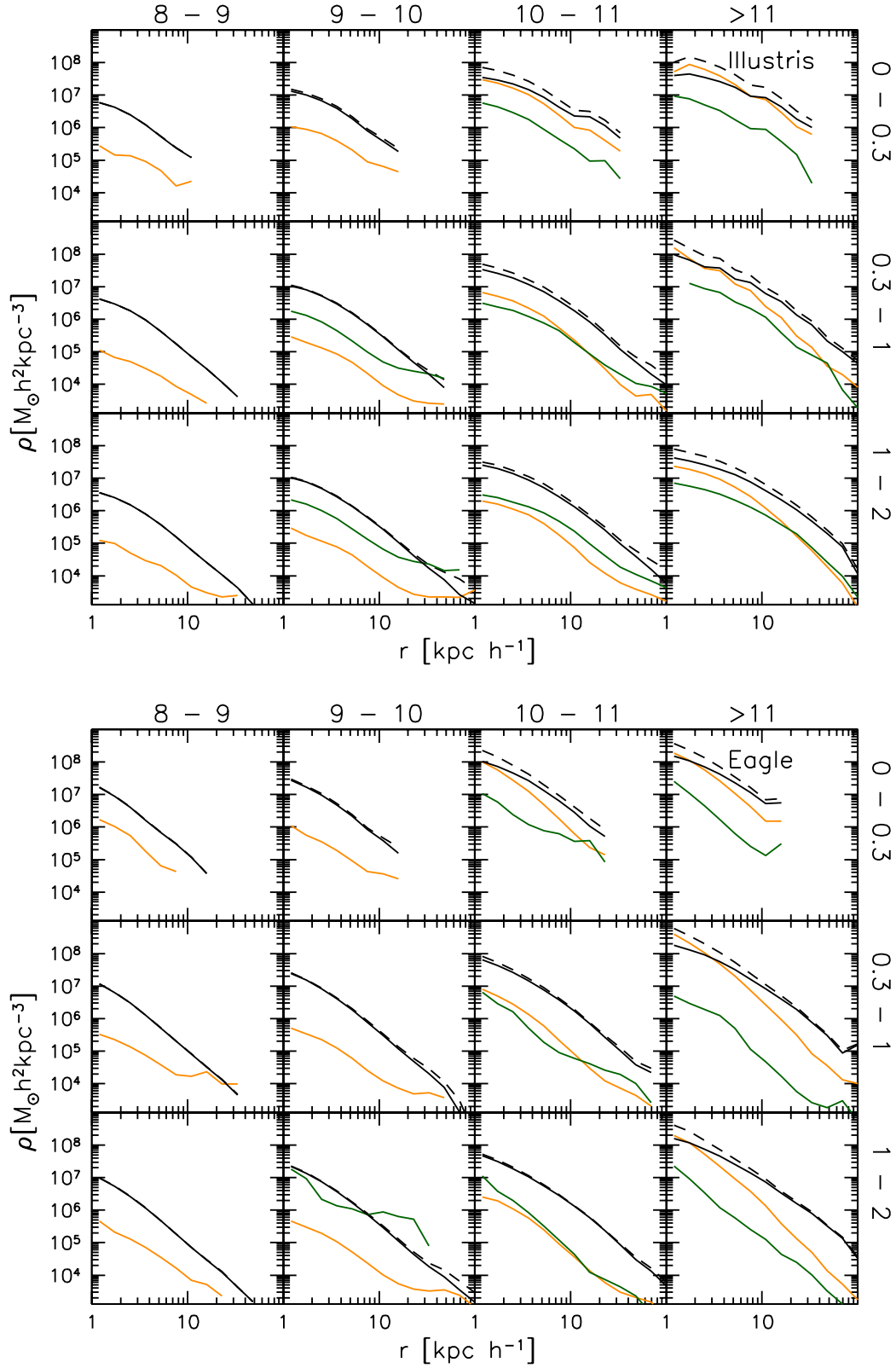


Figure 12. Mean density profile of the subhaloes belonging to the haloes in Figure 11, for different combination of subhalo mass (columns) and distance from the centre (rows) in units of r_{200c} . The colour scheme is the same of Figure 11. We note the same composition difference that was visible in Figure 10, with a different presence of stars and gas. Moreover, the effect of the accretion process is evident from the different extension of the subhaloes as we move towards the centre (from bottom to top).

can be found in projection in the central regions of the halo decreases by about one order of magnitude for each decade in subhalo mass.

We conclude that baryonic physics has an important impact on the halo structure and on the subhalo population; this needs to be taken into account when we compare predictions from simulations to observational results. The reduction in the number of small subhaloes is a clear consequence of the presence of baryons and of stellar and AGN feedback. However, in order to distinguish this effect from others, such as that of warm dark matter models (Lovell et al. 2014; Li et al. 2016), we need to reach lower subhalo mass. We plan to investigate these differences with zoom-in high resolution simulation in a follow-up paper.

The second part of this work focuses on the comparison with observational results, and in particular with the SLACS lenses. We searched for analogues in the simulations, considering ETGs which match the properties of the SLACS galaxies. We found a good number of these analogues at redshift between 0.2 and 0.5, selecting the galaxies by dynamical properties and velocity dispersion; we then verify that the selected galaxies lie in the right region of the $M_* - r_e$ plane and that the distribution of total stellar mass and virial mass are consistent with the observed ones. We use the selected galaxies to estimate detection probabilities with different physical models. For this, we make use of the sample of 11 SLACS lenses from Vegetti et al. (2014), among which only one substructure has been detected. We extract random samples of 11 SLACS-like haloes from the simulations and project their substructure on the sensitivity functions of the real lenses, in order to estimate how many subhaloes could be detected. We conclude that 1 detection of a mass $M > 10^9 M_\odot$ in a sample of 11 lenses is not a certain event, and it has a probability of 20 % (DMO), 19 % (EAGLE) or 10 % (Illustris). Many more observed lenses of ETG mass are needed to ensure a good number of detections and thus being able to fully constrain the subhalo mass function. We conclude by estimating the dark matter fraction in subhaloes within the areas of the sensitivity functions, which for the three models is f_{DM} (DMO, EAGLE, Illustris) = (0.0044, 0.0025, 0.0012). The values of (f_{DM}, α) from the DMO and from the EAGLE hydro runs are both compatible with the findings of Vegetti et al. (2014) within the errors.

This clearly shows that substructure lensing not only allows to distinguish between different dark matter models, but also between feedback and galaxy formation models, provided that the contribution of the line of sight clumps is well understood. This last aspect will be the main focus of a follow-up paper. Another scenario that needs to be addressed is that of different warm dark matter models, since it also causes a lack of low mass substructures; we plan to extend our findings to this and to the combination between warm dark matter and baryons in a future work, using higher resolution simulations in order to reach lower masses.

9 ACKNOWLEDGMENTS

We thank Dandan Xu, Simon White, Joop Schaye, Carlo Giocoli, Carlos Frenk, Rob Crain and Tom Theuns for useful discussions and comments. We thank Mark Lovell for providing some additional galaxy catalogues. We thank the

EAGLE collaboration for granting us access to the data for this project.

REFERENCES

- Auger M. W., Treu T., Bolton A. S., Gavazzi R., Koopmans L. V. E., Marshall P. J., Bundy K., Moustakas L. A., 2009, *ApJ*, 705, 1099
- Auger M. W., Treu T., Bolton A. S., Gavazzi R., Koopmans L. V. E., Marshall P. J., Moustakas L. A., Burles S., 2010b, *ApJ*, 724, 511
- Auger M. W., Treu T., Gavazzi R., Bolton A. S., Koopmans L. V. E., Marshall P. J., 2010a, *ApJ*, 721, L163
- Bennett C. L., Larson D., Weiland J. L., Jarosik N., Hinshaw G., Odegard N., Smith K. M., Hill R. S., et al. G., 2013, *ApJS*, 208, 20
- Blumenthal G. R., Faber S. M., Flores R., Primack J. R., 1986, *ApJ*, 301, 27
- Bolton A. S., Burles S., Koopmans L. V. E., Treu T., Moustakas L. A., 2006, *ApJ*, 638, 703
- Bryan G. L., Norman M. L., 1998, *ApJ*, 495, 80
- Crain R. A., Schaye J., Bower R. G., Furlong M., Schaller M., Theuns T., Dalla Vecchia C., Frenk C. S., McCarthy I. G., Helly J. C., Jenkins A., Rosas-Guevara Y. M., White S. D. M., Trayford J. W., 2015, *MNRAS*, 450, 1937
- Cui W., Borgani S., Dolag K., Murante G., Tornatore L., 2012, *MNRAS*, 423, 2279
- Dalal N., Kochanek C. S., 2002, *ApJ*, 572, 25
- Duffy A. R., Schaye J., Kay S. T., Dalla Vecchia C., Battye R. A., Booth C. M., 2010, *MNRAS*, 405, 2161
- Fiacconi D., Madau P., Potter D., Stadel J., 2016, *ArXiv e-prints*
- Giocoli C., Pieri L., Tormen G., 2008, *MNRAS*, 387, 689
- Giocoli C., Tormen G., Sheth R. K., van den Bosch F. C., 2010a, *MNRAS*, 404, 502
- Gnedin O. Y., Kravtsov A. V., Klypin A. A., Nagai D., 2004, *ApJ*, 616, 16
- Heitmann K., Lukić Z., Fasel P., Habib S., Warren M. S., White M., Ahrens J., Ankeny L., Armstrong R., O'Shea B., Ricker P. M., Springel V., Stadel J., Trac H., 2008, *Computational Science and Discovery*, 1, 015003
- Hezaveh Y. D., Dalal N., Marrone D. P., Mao Y.-Y., Morn-ingstar W., Wen D., Blandford R. D., Carlstrom J. E., Fassnacht C. D., Holder G. P., Kembell A., Marshall P. J., Murray N., Perreault Levasseur L., Vieira J. D., Wechsler R. H., 2016, *ApJ*, 823, 37
- Knebe A., Knollmann S. R., Muldrew S. I., Pearce F. R., Aragon-Calvo M. A., Ascasibar Y., Behrooz P. S., Ceverino D., et al. 2011, *MNRAS*, 415, 2293
- Knebe A., Pearce F. R., Lux H., Ascasibar Y., Behrooz P., Casado J., Moran C. C., Diemand J., et al. 2013, *MNRAS*, 435, 1618
- Li R., Frenk C. S., Cole S., Gao L., Bose S., Hellwing W. A., 2016, *MNRAS*
- Lovell M. R., Eke V., Frenk C. S., Gao L., Jenkins A., Theuns T., Wang J., White S. D. M., Boyarsky A., Ruchayskiy O., 2012, *MNRAS*, 420, 2318
- Lovell M. R., Frenk C. S., Eke V. R., Jenkins A., Gao L., Theuns T., 2014, *MNRAS*, 439, 300
- Ludlow A. D., Navarro J. F., Li M., Angulo R. E., Boylan-Kolchin M., Bett P. E., 2012, *MNRAS*, 427, 1322

- McAlpine S., Helly J. C., Schaller M., Trayford e. a., 2016, *Astronomy and Computing*, 15, 72
- Moster B. P., Somerville R. S., Maubetsch C., van den Bosch F. C., Macciò A. V., Naab T., Oser L., 2010, *ApJ*, 710, 903
- Nelson D., Pillepich A., Genel S., Vogelsberger M., Springel V., et al. T., 2015, *Astronomy and Computing*, 13, 12
- Neto A. F., Gao L., Bett P., Cole S., Navarro J. F., Frenk C. S., White S. D. M., Springel V., Jenkins A., 2007, *MNRAS*, 381, 1450
- Nierenberg A. M., Treu T., Wright S. A., Fassnacht C. D., Auger M. W., 2014, *MNRAS*, 442, 2434
- Onions J., Knebe A., Pearce F. R., Muldrew S. I., Lux H., Knollmann S. R., Ascasibar Y., Behroozi P., Elahi P., Han J., Maciejewski M., Merchán M. E., Neyrinck M., Ruiz A. N., Sgró M. A., Springel V., Tweed D., 2012, *MNRAS*, 423, 1200
- Planck Collaboration Ade P. A. R., Aghanim N., Alves M. I. R., Armitage-Caplan C., Arnaud M., Ashdown M., Atrio-Barandela F., Aumont J., Aussel H., et al. 2014, *A&A*, 571, A1
- Sawala T., Frenk C. S., Crain R. A., Jenkins A., Schaye J., Theuns T., Zavala J., 2013, *MNRAS*, 431, 1366
- Sawala T., Frenk C. S., Fattahi A., Navarro J. F., Bower R. G., Crain R. A., Dalla Vecchia C., Furlong M., Jenkins A., McCarthy I. G., Qu Y., Schaller M., Schaye J., Theuns T., 2015, *MNRAS*, 448, 2941
- Schaller M., Frenk C. S., Bower R. G., Theuns T., Jenkins A., Schaye J., Crain R. A., Furlong M., Dalla Vecchia C., McCarthy I. G., 2015, *MNRAS*, 451, 1247
- Schaye J., Crain R. A., Bower R. G., Furlong M., Schaller M., Theuns T., Dalla Vecchia C., Frenk C. S. e. a., 2015, *MNRAS*, 446, 521
- Snyder G. F., Torrey P., Lotz J. M., Genel S., McBride C. K., Vogelsberger M., Pillepich A., Nelson D., Sales L. V., Sijacki D., Hernquist L., Springel V., 2015, *MNRAS*, 454, 1886
- Springel V., 2010, *MNRAS*, 401, 791
- Springel V., Wang J., Vogelsberger M., Ludlow A., Jenkins A., Helmi A., Navarro J. F., Frenk C. S., White S. D. M., 2008, *MNRAS*, 391, 1685
- Springel V., White S. D. M., Frenk C. S., Navarro J. F., Jenkins A., Vogelsberger M., Wang J., Ludlow A., Helmi A., 2008, *Nature*, 456, 73
- Springel V., White S. D. M., Tormen G., Kauffmann G., 2001b, *MNRAS*, 328, 726
- Teklu A. F., Remus R.-S., Dolag K., Beck A. M., Burkert A., Schmidt A. S., Schulze F., Steinborn L. K., 2015, *ApJ*, 812, 29
- Vegetti S., Koopmans L. V. E., 2009, *MNRAS*, 392, 945
- Vegetti S., Koopmans L. V. E., Auger M. W., Treu T., Bolton A. S., 2014, *MNRAS*, 442, 2017
- Vegetti S., Koopmans L. V. E., Bolton A., Treu T., Gavazzi R., 2010, *MNRAS*, 408, 1969
- Vegetti S., Lagattuta D. J., McKean J. P., Auger M. W., Fassnacht C. D., Koopmans 2012, *Nature*, 481, 341
- Velliscig M., van Daalen M. P., Schaye J., McCarthy I. G., Cacciato M., Le Brun A. M. C., Dalla Vecchia C., 2014, *MNRAS*, 442, 2641
- Vogelsberger M., Genel S., Springel V., Torrey P., Sijacki D., Xu D., Snyder G., Nelson D., Hernquist L., 2014, *MNRAS*, 444, 1518
- Xu D., Sluse D., Gao L., Wang J., Frenk C., Mao S., Schneider P., Springel V., 2015, *MNRAS*, 447, 3189
- Xu D. e. a., 2016, in preparation
- Zhu Q., Marinacci F., Maji M., Li Y., Springel V., Hernquist L., 2016, *MNRAS*, 458, 1559